ChemComm

COMMUNICATION

View Article Online
View Journal | View Issue

Cite this: *Chem. Commun.*, 2026, **62**, 910

Received 14th May 2025,
Accepted 4th December 2025

DOI: 10.1039/d5cc02721g

rsc.li/chemcomm

Sintering of W-substituted Na_3SbS_4 electrolytes: effect of phase composition, voids, and interface contact

Fuwei Wen, Xiang You, Geng Xie, Arthur Mar and Lingzi Sang *

Tungsten-substituted Na_3SbS_4 shows enhanced ionic conductivity but the role of sintering treatments is not well understood. The effects of sintering on $Na_{3-x}Sb_{1-x}W_xS_4$ were examined and found to slightly increase the solubility of W, reduce voids, and possibly increase contact area. Changes in phase composition and morphology play a key role in the performance of $Na_{3-x}Sb_{1-x}W_xS_4$ electrolytes.

W-Substituted Na_3SbS_4 (WNSS) has attracted significant attention as a potential electrolyte for all-solid-state sodium batteries.[1,2] Na_3SbS_4 already exhibits a high Na^+ conductivity of 1.1 mS cm^{-1}, comparable to liquid electrolytes, and is stable in dry air.[1,3–6] Because it is synthesized in aqueous media, it can be readily adapted for solution processing of solid composite electrolytes.[3,7] Among various chemical substitutions of the cation (Sb^{5+}) or the anion (S^{2-}),[8–12] W substitution greatly enhances the Na^+ conductivity in Na_3SbS_4.[13,14] At the limiting solubility of 12% W, $Na_{2.88}Sb_{0.88}W_{0.12}S_4$ exhibits a higher Na^+ conductivity of 41 ± 8 mS cm^{-1}, which has been attributed to vacancies created by substitution of Sb^{5+} by W^{6+} to maintain charge neutrality.[15–21] This substitution also causes a unit cell expansion, which was correlated with the improved conductivity.[16] Somewhat contradictory results were reported in which orthorhombic $Na_{2.895}Sb_{0.7}W_{0.3}S_4$, at an even higher level of W substitution (30%), exhibits a Na^+ conductivity of 24.2 mS cm^{-1}; beyond 30%, Na^+ impeding phases and diminished conductivity were observed.[22] Although not definitively identified in this report, these phases likely include WS_2 and $NaSbS_2$, according to databases.[23] There is thus a need to clarify the extent of W solubility in Na_3SbS_4 and the nature of these Na^+ impeding phases as they emerge.

Sintering at high temperatures of WNSS has been commonly applied after synthesis, although the effects of this process have not been directly examined. It is not clear if the sintering process induces changes in W solubility or formation of secondary phases, which would affect Na^+ conductivity. In other more extensively reported cases, sintering of garnet, NASICON, and sulfide solid electrolytes increases crystallinity and reduces grain boundary resistance by eliminating voids.[24–35] Sintering causes solid electrolyte pellets to be densified, which promotes ionic transport between domains and improves contact between electrode and electrolyte.[25,27–29,31,34–37] For example, $Li_{1.3}Al_{0.3}Ti_{1.7}(PO_4)_3$ was sintered in two steps at low (120 °C) and high temperature (650 °C) to enhance the contact between domains.[33] Sintering parameters include temperature, duration, and atmospheric conditions. For optimal densification and contact, the temperature should be precisely kept just below the deformation temperature of the solid electrolyte pellet. For example, Mg-substituted NASICON was optimally sintered at 1250 °C; slightly higher temperature (1300 °C) deformed the pellet while slightly lower temperature (1200 °C) gave microcracks from thermal shrinkage.[38] WNSS was sintered at 500 °C, which is below the melting temperature of 550 °C.[16] Optimal sintering conditions depend highly on phase transitions and thermal stability of the specific material.[39]

The phase composition and microscopic-level pellet morphology are the two parameters that directly impact the Na^+ conductivity of the WNSS electrolyte and the contact between WNSS and the electrode materials. An in-depth understanding of the effect of sintering on the aforementioned two parameters is required for producing WNSS solid–electrolyte pellet that supports the optimal Na^+ conductivity and interfacial contact. In this work, we investigated the impact of post-synthesis sintering in WNSS by characterizing the composition, chemical heterogeneity, and ionic conductivity using powder X-ray diffraction (XRD), Raman spectroscopy, and electrochemical impedance spectroscopy (EIS), with an aim to establish a clearer correlation between W solubility and ionic conductivity. After sintering, the bulk morphology of a WNSS electrolyte pellet and its contact with a Na electrode were examined.

Several samples of $Na_{3-x}Sb_{1-x}W_xS_4$ were synthesized with nominal compositions at x = 0.12, 0.16, 0.24, and 0.32 (labeled as WNSS-12, -16, -24, -32) and sintered at 500 °C. The powder XRD patterns of as-synthesized and sintered samples appear similar at first glance over the entire range (2θ = 5–90°) (Fig. 1A).

Department of Chemistry, University of Alberta, Edmonton, Alberta, T6G 2G2, Canada. E-mail: lsang@ualberta.ca

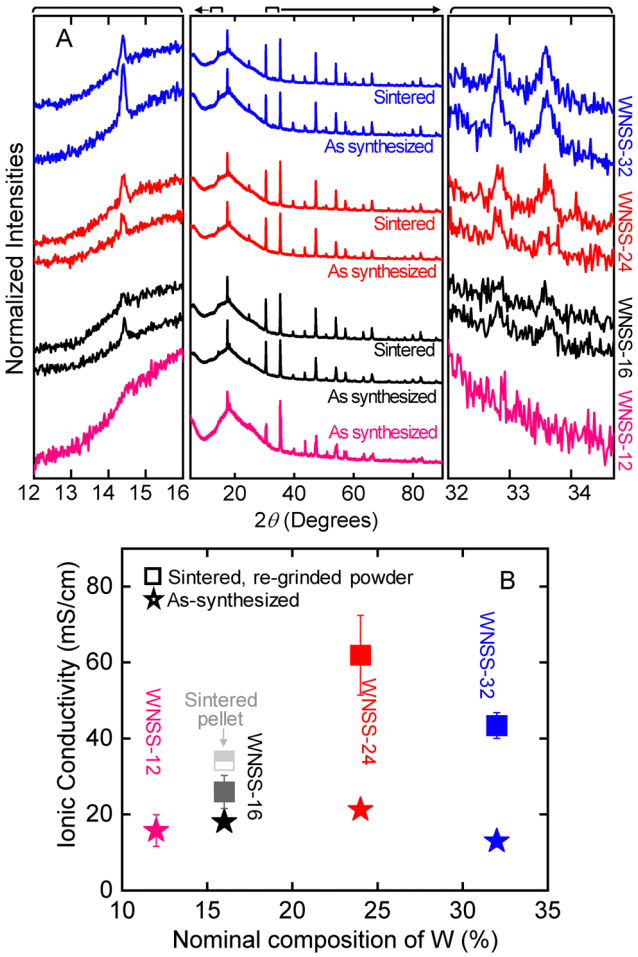

Fig. 1 (A) Powder XRD patterns of as-synthesized and 500 °C sintered WNSS samples, with regions at 12–16° and 32–35° highlighted. Intensities were normalized to the peak at 30.4° in 2θ. (B) Ionic conductivity of as-synthesized and sintered WNSS samples.

Experimentally measured and simulated diffraction patterns of Na_3SbS_4 were provided in Fig. S1 for reference. Closer inspection shows several peaks assigned to the 002(14.68°), 100(32.80°), and 101(33.64°) reflections of WS_2 present as a secondary phase in all samples except as-synthesized WNSS-12.[9] As the nominal W composition increases beyond x = 0.12, WS_2 becomes more prominent in the as-synthesized samples. Sintering tends to reduce the amount of WS_2 (except for WNSS-24) but the conclusions are a little unclear from this information alone.

To gain some insight about the possible phase heterogeneity of the samples, Raman scattering signals were compared for an average over a large area *vs.* randomly selected localized spots. Over a large sampling area (50 μm spot diameter), the samples showed similar Raman spectra before and after sintering (Fig. S2). Aside from the unknown peaks associated with WNSS decomposition, assignments of vibrational signatures of WNSS and the common secondary phase WS_2 were provided in our previous work.[40] The spectra agree with previous reports for WNSS-12.[16,40] Raman shifts at 350 and 420 cm^{-1} characteristic of WS_2 were not observed in any sample,[41,42] in seeming contradiction with the XRD data. This discrepancy could be explained by small domain sizes of WS_2 which would exhibit a limited scattering cross-section under the low photon intensity distributed over the large incident beam. Over a much smaller sampling area (1.3 μm focused beam diameter), the as-synthesized WNSS-16, -24, and -32 samples showed variations in Raman spectra collected over 5–6 spots, implying heterogeneity (Fig. S3). After these samples were sintered and reground, the Raman spectra became identical across 6 spots for WNSS-16 and 24, implying improved homogeneity, but were still slightly inconstant for WNSS-32 (Fig. S4). Without grinding, the surfaces of all sintered pellets were highly heterogeneous (Fig. S5).

The Na^+ conductivities of as-synthesized *vs.* sintered and reground WNSS powders were measured (Fig. 1B). Nyquist plots obtained from the EIS measurements and calculation examples for extracting Na^+ conductivities were provided in the SI (Fig. S6, S7 and Table S1). Among the as-synthesized samples, the ionic conductivities were 15–18 mS cm^{-1} for WNSS-12 and -16 (comparable to previously reported values),[13,14,16] slightly higher for WNSS-24, and lower for WNSS-32. This trend is consistent with the formation of WS_2, which acts to block Na^+ conduction, seen in the XRD and Raman results beyond the limiting solubility of W. In general, sintering improves the ionic conductivity. One possible explanation is that sintering improves W solubility but this hypothesis was contradicted by the XRD results specifically for the sintered WNSS-24 sample, which actually contains increased amounts of WS_2. Sintered WNSS-24 also shows higher conductivity than sintered WNSS-16 even though it contains more WS_2. These discrepancies suggest that other factors may be at play. In particular, sintering reduces voids, which would enhance inter-particle contact and improve Na^+ mobility between particles. For example, WNSS-16 shows higher conductivity before regrinding and repelletizing.

To examine the bulk morphology and voids of as-synthesized and sintered WNSS samples, SEM images of pellet cross-sections were acquired by stepwise ion milling using a plasma-focused ion beam. Experimental details are provided in the SI. SEM images of the interior of WNSS-16 pellets were taken at various stages of ion milling (Fig. 2). By gradually milling across the pellet, these images display the cross-section in increments of 0.3 μm. The uppermost 2–3 μm of both as-synthesized and sintered pellets show porous characteristics resulting from unavoidable decomposition when the samples were briefly exposed to moisture during transfer to the analysis chamber. Nevertheless, the cross-sections of the pellets are markedly different in the as-synthesized *vs.* sintered samples. The as-synthesized pellets contained prominent voids (highlighted by red arrows) whereas the sintered pellets showed consistently dense cross-sections. This result confirms that sintering does reduce voids, densifying the pellets and improving ionic conductivity as observed above. The density of WNSS-16 pellets before and after sintering was also estimated from the mass and volume. The result was provided in the SI. Shown in Table S2, following sintering, the density of a WNSS-16 pellet was estimated to be 2.721 ± 0.007 g cm^{-3} compared to 2.670 ± 0.007 g cm^{-3} measured from samples before sintering. This estimation is consistent with the reduced

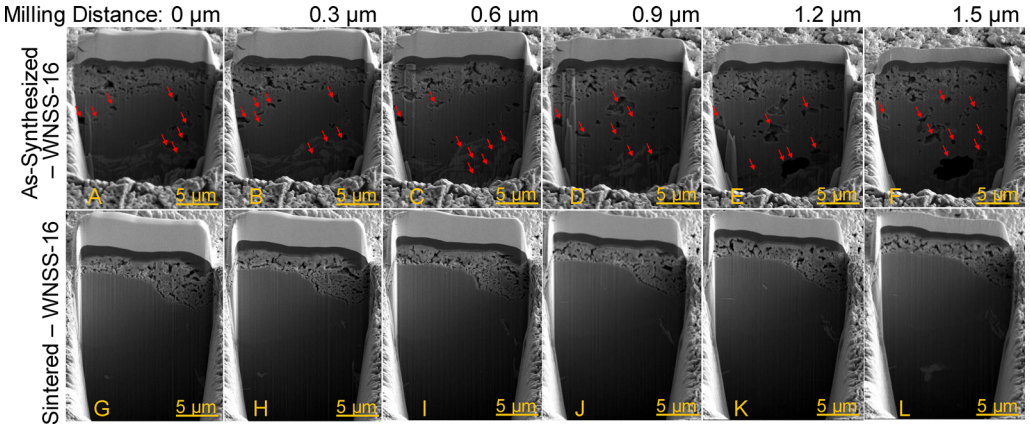

Fig. 2 SEM images obtained from the cross-sections of (A)–(F) as-synthesized and (G)–(L) sintered WNSS-16 pellets with various FIB milling distances. Red arrows indicate the presence of voids inside the pellets.

pores and voids observed from the cross-sectional FIB-SEM results. The porous layer in sintered pellets was also significantly thinner than in as-synthesized pellets, suggesting that sintering suppresses moisture penetration during brief air exposure.

To examine the effect of sintering on the physical contact between the Na electrode and WNSS pellet surface, Na/WNSS-16/Na was cycled galvanostatically using a 0.10 mA cm^{-2} current density. As reported previously, WNSS is prone to chemical or electrochemical reduction at the Na surface, yielding a Na^+ insulating layer that increases overall cell resistivity over cycling.[4,40] The decomposition layer likely consists of Na_xSb and WS_2, among other by-products.[4] The application of WNSS as solid electrolytes for sodium batteries requires further understanding of this decomposition chemistry and the approach to suppress it, which is beyond the scope of this work. Herein, we used this decomposition phenomenon to assess the Na/WNSS contact in the as-synthesized and sintered WNSS samples. The cycling performances of symmetric cells containing as-synthesized *vs.* sintered WNSS-16 pellets were compared.

The cell containing sintered WNSS-16 shows a more drastic increase in redox overpotential compared to the as-synthesized WNSS-16 (Fig. 3A and B). Given the presence of WNSS deposition, this relatively higher magnitude in overpotential suggests enhanced contact at the Na/WNSS interface, forming more Na^+ blocking decomposition products at the interface. Consistently, a more significant increase of impedance was seen in cells containing sintered WNSS-16 compared to the as-synthesized samples (Fig. 3D), although the overall cell impedance was comparable before cycling (Fig. 3C). This increase of interfacial impedance was quantified by assuming that the intrinsic conductivity of WNSS-16 remains unchanged during cycling, while the overall "apparent" increased interfacial resistance (R_{int}) extracted from fitting the EIS data may involve contributions from multiple interfacial components which cannot be deconvoluted from the Nyquist plots. The equivalent circuit model employed in this analysis was provided in Fig. S8 along with the summarized results provided in Table S3. The obtained R_{int} was plotted over cycles for the two samples (Fig. 3E). The substantial increase in R_{int} for sintered WNSS-16 suggests that a more

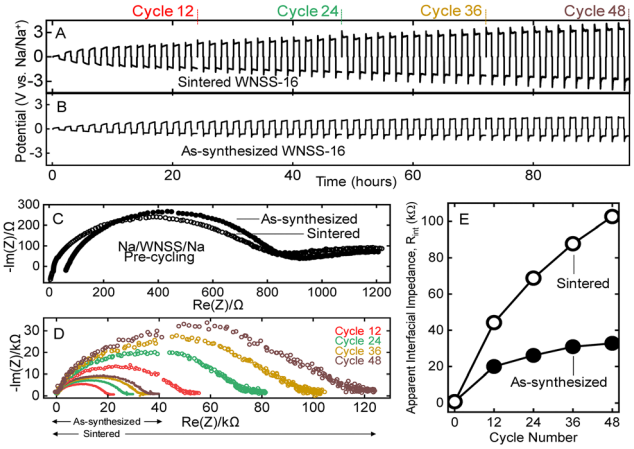

Fig. 3 Galvanostatic charge/discharge cycles obtained from Na/WNSS-16/Na cells when (A) 500 °C sintered and (B) as-synthesized WNSS-16 were used for cell assembly. EIS obtained from the Na/WNSS-16/Na cells (C) before and (D) following cycles 12, 24, 36, and 48. (E) Apparent interfacial impedance before and after cycles 12, 24, 36, and 48 in symmetric cells containing as-synthesized *vs.* sintered WNSS-16.

intimate contact may be present at the Na/sintered-WNSS-16 interface. Cyclic voltammetry results and the cell impedance obtained from the same symmetric cells containing as-synthesized and sintered WNSS-16 were also compared. Although the cell containing sintered WNSS-16 shows higher current density at cycle 1 due to the higher ionic conductivity of electrolytes (Fig. S9), the impedance growth was more significant in sintered samples (Fig. S10). At the microscopic level, this intimate contact can be provided by a smoother pellet surface or an improved Na wettability. Because the chemical composition of the pellet surface of the sample was similar before and after sintering, the pellet morphology likely dominates the microscopic contact area. Aside from the marked contrast in the overpotential observed during galvanostatic charge/discharge cycles, an instantaneous voltage spike was also noted at the beginning of charge and discharge segments, indicating the formation of a stabilized space charge layer at the interface after about 10 cycles for both as-synthesized and

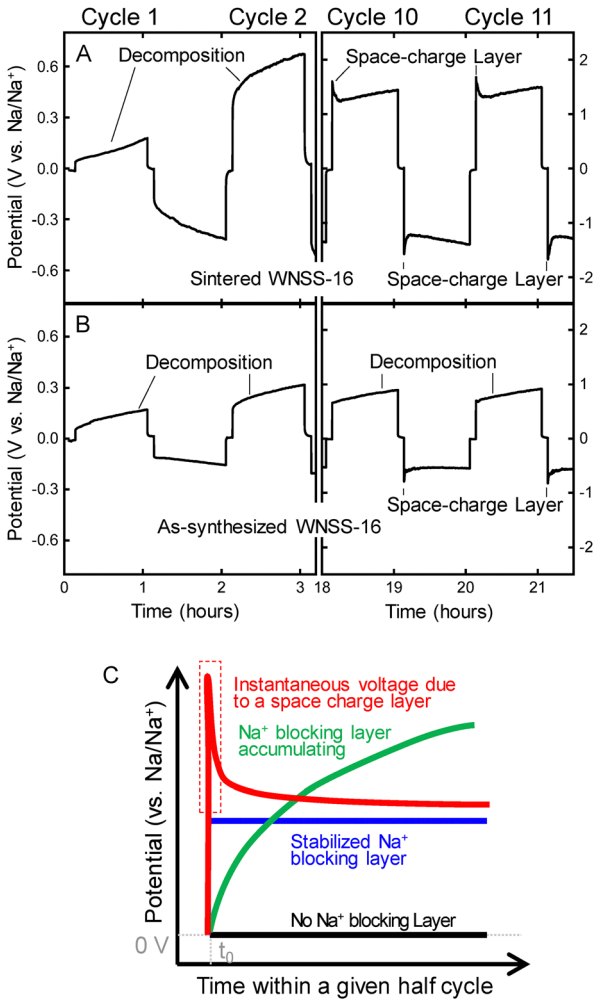

Fig. 4 Galvanostatic charge/discharge curve of cycles 1–2, and 10–11 cycles in Na/WNSS/Na cells containing (A) sintered WNSS and (B) as-synthesized WNSS, (C) three possible types of potential *vs.* cycle time behaviour within one redox half cycle and their correlation with the decomposition process occurring at the Na/WNSS interface.

sintered samples (Fig. 4). Consistent with previous findings, Na_2S was found as one major interfacial by-product that contributes to the increased cell resistivity (Fig. S11 and S12).

In conclusion, sintering of $Na_{3-x}Sb_{1-x}W_xS_4$ samples led to a slight increase in the W solubility from 12% to 16%, as suggested by lower amounts of WS_2 secondary phase in sintered WNSS-16. The sintered pellets showed substantially fewer voids, and this densification was likely the dominating factor for increased ionic conductivity in all sintered WNSS samples. Sintering also led to smoother surfaces, which results in increased contact area between WNSS and the Na electrode; this phenomenon, in consequence, yields more severe WNSS reduction at the WNSS/Na interface.

The manuscript was written with the contributions of all authors. All authors have given approval to the final version of the manuscript. F. W. conducted materials preparation and performed XRD, Raman measurements. F. W. and G. X. performed electrochemical characterization and data analysis. F. W. and X. Y. conducted electron microscopy measurements. A. M. and L. S. supported data interpretation and oversaw the project.

Conflicts of interest

The authors declare no conflict of interest.

Data availability

The data supporting this article have been included as part of the supplementary information (SI). Supplementary information is available. See DOI: https://doi.org/10.1039/d5cc02721g.

References

1 H. Wang, Y. Chen, Z. D. Hood, G. Sahu, A. S. Pandian, J. K. Keum, K. An and C. Liang, *Angew. Chem., Int. Ed.*, 2016, **55**, 8551–8555.
2 A. Banerjee, K. H. Park, J. W. Heo, Y. J. Nam, C. K. Moon, S. M. Oh, S.-T. Hong and Y. S. Jung, *Angew. Chem., Int. Ed.*, 2016, **55**, 9634–9638.
3 S. Dong, G. Xie, S. Xu, X. Tan, M. Chaudhary, Y. Zhang, R. Wu, F. Wen, C. Ayranci, V. K. Michaelis, A. Quirk, S. M. Rosendahl, J. Liu, M. D. Fleischauer and L. Sang, *ACS Nano*, 2024, **18**, 16285–16296.
4 G. Xie, M. Tang, S. Xu, A. Brown and L. Sang, *ACS Appl. Mater. Interface*, 2022, **14**, 48705–48714.
5 Q. Zhang, C. Zhang, Z. D. Hood, M. Chi, C. Liang, N. H. Jalarvo, M. Yu and H. Wang, *Chem. Mater.*, 2020, **32**, 2264–2271.
6 M. Shimoda, M. Maegawa, S. Yoshida, H. Akamatsu, K. Hayashi, P. Gorai and S. Ohno, *Chem. Mater.*, 2022, **34**, 5634–5643.
7 C. He, C. Gao, J. Zhang, X. Li, T. Zhou, S. Kang, L. Tan, Q. Jiao and C. Lin, *J. Am. Ceram. Soc.*, 2024, **107**, 188–194.
8 Z. Gong, L. Shu, J. Yin, C. Gao, Y. Liu, X. Zhou, X. Shen, S. Dai, C. Lin and Q. Jiao, *J. Mater. Chem. C*, 2023, **11**, 15967–15978.
9 Y. Shen, T. Huan, J. Lu, C. Gao, Y. Liu, S. Dai, C. Lin, X. Zhang, H. Ma, X. Shen and Q. Jiao, *J. Am. Ceram. Soc.*, 2025, **108**, e20379.
10 R. Jalem, B. Gao, H.-K. Tian and Y. Tateyama, *J. Mater. Chem. A*, 2022, **10**, 2235–2248.
11 C. He, C. Gao, J. Zhang, X. Li, T. Zhou, W. Tao, S. Kang, L. Tan, Q. Jiao, S. Dai and C. Lin, *Ceram. Int.*, 2024, **50**, 2541–2548.
12 T. Huan, J. Yin, Y. Shen, J. Lu, C. Gao, Y. Liu, S. Dai, C. Lin, X. Zhang, H. Ma, X. Shen and Q. Jiao, *J. Mater. Chem. C*, 2024, **12**, 19296–19306.
13 A. Hayashi, N. Masuzawa, S. Yubuchi, F. Tsuji, C. Hotehama, A. Sakuda and M. Tatsumisago, *Nat. Commun.*, 2019, **10**, 5266.
14 S. Yubuchi, A. Ito, N. Masuzawa, A. Sakuda, A. Hayashi and M. Tatsumisago, *J. Mater. Chem. A*, 2020, **8**, 1947–1954.
15 R. Jalem, A. Hayashi, F. Tsuji, A. Sakuda and Y. Tateyama, *Chem. Mater.*, 2020, **32**, 8373–8381.
16 T. Fuchs, S. P. Culver, P. Till and W. G. Zeier, *ACS Energy Lett.*, 2020, **5**, 146–151.
17 M. Ravalli, M. Soleimanzade, M. Scavini, S. C. Tarantino, M. Radaelli and C. Tealdi, *J. Mater. Chem. A*, 2024, **12**, 31861–31870.
18 O. Maus, M. T. Agne, T. Fuchs, P. S. Till, B. Wankmiller, J. M. Gerdes, R. Sharma, M. Heere, N. Jalarvo, O. Yaffe, M. R. Hansen and W. G. Zeier, *J. Am. Chem. Soc.*, 2023, **145**, 7147–7158.
19 C.-W. Lee, M. Maegawa, H. Akamatsu, K. Hayashi, S. Ohno and P. Gorai, *ACS Mater. Lett.*, 2025, **7**, 620–626.
20 J. Klarbring and A. Walsh, *Chem. Mater.*, 2024, **36**, 9406–9413.
21 J. G. Smith and D. J. Siegel, *Chem. Mater.*, 2022, **34**, 4166–4171.
22 X. Feng, H. Fang, P. Liu, N. Wu, E. C. Self, L. Yin, P. Wang, X. Li, P. Jena, J. Nanda and D. Mitlin, *Angew. Chem., Int. Ed.*, 2021, **60**, 26158–26166.
23 K. Cenzual, L. M. Gelato, M. Penzo and E. Parthé, *Acta Crystallogr., Sect. B: Struct. Sci.*, 1991, **47**, 433–439.
24 L. Shen, J. Yang, G. Liu, M. Avdeev and X. Yao, *Mater. Today Energy*, 2021, **20**, 100691.
25 A. C. Radjendirane, D. K. Maurya, J. Ren, H. Hou, H. Algadi, B. B. Xu, Z. Guo and S. Angaiah, *Langmuir*, 2024, **40**, 16690–16712.
26 L. Yang, X. Huang, C. Zou, X. Tao, L. Liu, K. Luo, P. Zeng, Q. Dai, Y. Li, L. Yi, Z. Luo and X. Wang, *Ceram. Int.*, 2021, **47**, 18196–18204.

27 T. Ortmann, S. Burkhardt, J. K. Eckhardt, T. Fuchs, Z. Ding, J. Sann, M. Rohnke, Q. Ma, F. Tietz, D. Fattakhova-Rohlfing, C. Kübel, O. Guillon, C. Heiliger and J. Janek, *Adv. Energy Mater.*, 2023, **13**, 2202712.
28 Y. Xing, Y. Li and C. Zhang, *Solid State Ionics*, 2021, **373**, 115811.
29 A. Sazvar, M. Hajibandeh, P. Vafaei, E. Hosseinzadeh and M. Jabbari, *J. Energy Storage*, 2024, **101**, 113863.
30 W. Sun, Y. Li, C. Sun, Z. Sun, H. Jin and Y. Zhao, *Batteries*, 2024, **10**, 359.
31 P. Jiang, G. Du, Y. Shi, F. She, P. Guo, G. Qian, X. Lu, F. Xie and X. Lu, *Chem. Eng. J.*, 2023, **451**, 138771.
32 Z. M. Grady, K. Tsuji, A. Ndayishimiye, J. Hwan-Seo and C. A. Randall, *ACS Appl. Energy Mater.*, 2020, **3**, 4356–4366.
33 Y. Liu, J. Liu, Q. Sun, D. Wang, K. R. Adair, J. Liang, C. Zhang, L. Zhang, S. Lu, H. Huang, X. Song and X. Sun, *ACS Appl. Mater. Interface*, 2019, **11**, 27890–27896.
34 S. Yang, Y. Tang, Y. Yao, S. He, Z. Wu, Y. Yang, H. Pan, X. Rui and Y. Yu, *Mater. Horiz.*, 2025, **12**, 1058–1083.
35 X. Guo, S. Halacoglu, Y. Chen and H. Wang, *Small*, 2024, **20**, 2311195.
36 M. Balaish, J. C. Gonzalez-Rosillo, K. J. Kim, Y. Zhu, Z. D. Hood and J. L. M. Rupp, *Nat. Energy*, 2021, **6**, 227–239.
37 I. D. Seymour and A. Aguadero, *J. Mater. Chem. A*, 2021, **9**, 19901–19913.
38 A. Chakraborty, R. Thirupathi, S. Bhattacharyya, K. Singh and S. Omar, *J. Power Sources*, 2023, **572**, 233092.
39 R. Kan, Y. Xu, R. Chen, M. Jiang, B. Fu, C. Song, P. Tao, J. Wang, T. Deng and W. Shang, *Energy Storage Mater.*, 2024, **68**, 103366.
40 F. Wen, G. Xie, N. Chen, Q. Wu, M. Chaudhary, X. You, V. K. Michaelis, A. Mar and L. Sang, *ACS Appl. Mater. Interface*, 2023, **15**, 40070–40079.
41 H. Zobeiri, S. Xu, Y. Yue, Q. Zhang, Y. Xie and X. Wang, *Nanoscale*, 2020, **12**, 6064–6078.
42 A. A. Mitioglu, P. Plochocka, G. Deligeorgis, S. Anghel, L. Kulyuk and D. K. Maude, *Phys. Rev. B: Condens. Matter Mater. Phys.*, 2014, **89**, 245442.